

Detailed physical property characterization of $\text{FeTe}_{1-x}\text{Se}_x$ ($0.00 \leq x \leq 0.50$) single crystals

P.K. Maheshwari^{1,2}, V. Raghavendra Reddy³, Bhasker Gahtori¹ and V.P.S. Awana^{1, 2,*}

¹CSIR-National Physical Laboratory, Dr. K. S. Krishnan Marg, New Delhi-110012, India

²Academy of Scientific and Innovative Research (AcSIR), Ghaziabad- 201002, India

³UGC-DAE Consortium for Scientific Research, Khandwa Road, Indore-425001, India

Abstract

Here, we report self flux single crystal growth of $\text{FeTe}_{1-x}\text{Se}_x$ ($0.00 \leq x \leq 0.50$) series via solid state reaction route; the resulted crystals as seen are shiny. X-Ray diffraction (XRD) performed on the surface of crystals elucidated the growth in (00 l) plane, i.e. orientation in c -direction only. Scanning electron microscopy (SEM) images showed slab like morphology and EDX (Energy dispersive X-ray analyzer) confirmed that the crystals are closed to their designed compositions. Rietveld analysis of the XRD patterns of crushed crystal powders showed that the cell parameters decrease with Se content increase. Coupled magnetic/structural phase transition temperature, seen as a step in resistivity for the lower Se concentration i.e. $0.00 \leq x \leq 0.07$, decreases from around 65K for $x=0.0$ to 50K for $x=0.07$ and it is not detected for higher x values. Superconductivity is observed by resistivity measurement for higher Se concentration i.e. $0.07 \leq x \leq 0.50$, up to a maximum temperature of 14K at $x=0.50$. Thermally Activated Flux Flow (TAFF) analysis based on high field transport measurements in superconducting region done for $x=0.20$ crystal exhibited activated flux energy to be decreasing from 12meV (0.5Tesla) to 4.6meV (14Tesla). Raman spectroscopy at room temperature of synthesized samples exhibits all the allowed phonon modes with slight shift to higher frequency with Se content. Mossbauer spectra of $\text{FeTe}_{1-x}\text{Se}_x$ crystals series were recorded at 300 and 5K. At 5K, the average hyperfine field decreases systematically with Se content increase from 10.6 to 6.1Tesla for $x=0.0$ to $x=0.20$ samples. This indicates a possibility of co-existing magnetism and superconductivity in $0.07 \leq x \leq 0.20$ crystals. For $x=0.50$ sample, no hyperfine field related to magnetic ordering is seen. Based on above results, detailed phase diagram of the $\text{FeTe}_{1-x}\text{Se}_x$ ($0.00 \leq x \leq 0.50$) compounds is defined in the present study.

Key words: Fe chalcogenide Single crystals, Superconductivity and Structural details and magneto transport, Raman spectrum, Mossbauer spectra

***Corresponding Author**

Dr. V. P. S. Awana: E-mail: awana@nplindia.org
Ph. +91-11-45609357, Fax-+91-11-45609310
Homepage awanavps.webs.com

Introduction

Fe chalcogenide superconducting compounds [1, 2] possess the simplest PbO-type crystal structure among the Iron based superconducting family [1-6]. Because of their simplest crystal structure, having only Fe chalcogen layers, these are thought to be the ideal candidates for understanding the properties and mechanism of Fe based superconducting compounds [1-6]. The FeSe/As tetrahedral layers in Fe containing superconducting compounds are the key component, which play the role similar to that of CuO₂ layers in superconducting cuprates [7, 8]. As reported, doping of S/Se at Te site in PbO-type FeTe_{1-x}Se_x suppresses the magnetic ordering of parent Anti-ferromagnetic (AFM) compound FeTe and induces superconductivity [9-13]. The ground state of Iron Chalcogenides i.e. FeTe compound orders anti-ferro-magnetically below 70K [9, 14-16]. At ambient conditions, maximum T_c for Fe chalcogenides superconducting system is found to be 15K at x=0.50 [9, 16] and T_c was increased to 37K by hydraulic pressure [17-18]. T_c can be further increased up to 50K with favorable alkali metal (Na, Eu, Ca etc) intercalation [19-21].

Till now, the concept of superconductivity in Fe based compounds i.e. Fe chalcogenides and pnictides is not yet clear as T_c for these compounds gets increased of up to 100K for FeSe mono layer [22, 23], which cannot be explained by electron-phonon coupling theory and hence are termed as unconventional superconductors [24,25]. Because the electron-phonon coupling in FeSe/Te system is found to be weak, the phenomenon behind its superconductivity is yet challenging. Raman spectroscopy on single crystals of appropriate quality may provide some important information related to the electron coupling in these types of compounds [26]. Further, because a single crystal has no grain boundary related problems and, hence, it is always desired by condensed matter physicists for physical property measurements and theoretical modelling.

Till date, FeSe based compounds has no universal accepted phase diagram because of its phase complexity, as, in this system several phases and different crystal structures are appeared simultaneously. According to the defined phase diagram of FeSe system, it is not easy to obtain the

large-size single crystals of superconducting FeSe by the melt process technique [27]. On the other hand, the single crystal growth is relatively easy using simple melt process technique for Te substituted FeSe system [25, 28]. Here, we report the self flux growth of $\text{FeTe}_{1-x}\text{Se}_x$ ($0.00 \leq x \leq 0.50$) single crystals and their structural properties, superconducting property, Raman spectroscopy and Mossbauer spectra. When the temperature is decreased from 300K to 2K during resistivity measurements, the pure and some doped sample i.e. $x=0$ to 0.07 showed step like transition (coupled magnetic/structural) decreasing from 65K to 50K for $x=0.00$ to $x=0.07$, respectively. Other crystals show superconducting transition at low temperature and maximum T_c (14K) is achieved for $x=0.50$ sample. Interestingly, the $x=0.07$ crystal showed both the magnetic/structural and superconducting transitions at temperature around 50 and 10K, respectively. In Raman spectra, all the phonon modes are identified in low frequency range with slight higher frequency shift with Se doping. Mossbauer spectra data showed that the higher Se doping suppress the magnetic ordering in $\text{FeTe}_{1-x}\text{Se}_x$ series and some crystals do have both magnetic and superconductivity co-existing. Worth mentioning is the fact that, beyond $x=0.50$, the crystals could not be grown and the easy and versatile simple melt process technique did not work.

Experimental Details

The $\text{FeTe}_{1-x}\text{Se}_x$ ($0.00 \leq x \leq 0.50$) single crystals series are grown in a common programmable automated furnace without any extra added flux and complicated heating algorithm. All the essential elements i.e., Fe, Se and Te powders of high purity (better than 4N) from Sigma Aldrich are taken in their stoichiometric ratio i.e., $\text{FeTe}_{1-x}\text{Se}_x$ ($0.00 \leq x \leq 0.50$) and grinded separately in high purity Ar gas filled glove box. The grinded powders are pelletized by hydrostatic pressure of 100kg/cm^2 , and sealed separately in respective quartz tubes with the vacuum of better than 10^{-3}Torr . These sealed quartz tubes were kept in a programmable automated furnace and heated up to 1000°C for 24 hours with an intermediate step of 450°C at cooling rate of 2°C/minute . Finally the furnace was cool down very slowly up to room temperature with the cooling rate of 10°C/hour . The obtained crystals from furnace were very shiny. XRD of as obtained single crystals and their crushed powders was done using Rigaku X-ray diffractometer with CuK_α radiation of 1.541\AA at room temperature. SEM image and EDX had been taken on ZEISS-EVO-10 electron microscope to understand the morphology and elemental composition of $\text{FeTe}_{1-x}\text{Se}_x$ single crystals. Electrical and magnetic measurements were performed on Quantum Design Physical Property Measurement System (PPMS-14Tesla) down to 2K and up to magnetic field of 14Tesla. Raman spectra were recorded for all the samples at ambient condition on Renishaw Raman spectrometer

with excitation by laser beam of 514nm wavelength. ^{57}Fe Mossbauer measurements were performed on crushed powder samples having ^{57}Co radioactive source in transmission mode. Mossbauer spectra have been recorded using WissEl velocity drive, calibrated at room temperature with natural Iron absorber, and at low temperature measurements were performed using the Janis made superconducting magnet.

Results and Discussion

Single crystal XRD of $\text{FeTe}_{1-x}\text{Se}_x$ ($0.00 \leq x \leq 0.50$) series were performed at room temperature and obtained XRD patterns are shown in figure 1. From figure 1, it may be clearly seen that direction of crystal growth is in $[00l]$ plane orientation i.e. in c direction, being as the highest peak intensities of XRD pattern are only occurring by (001), (002) and (003) planes, in 2θ range of 10 to 55° . This result impounds the single crystalline nature of the studied crystals. For generality, it can be mentioned that atom layer stack formation and XRD patterns of similar type were observed for other layered chalcogenide crystals [29-31]. Also, it can be concluded that c cell parameter decreases monotonically with increasing Se doping at Te site, as the position of (00 l) plane is shifted to higher angle in 2θ graph.

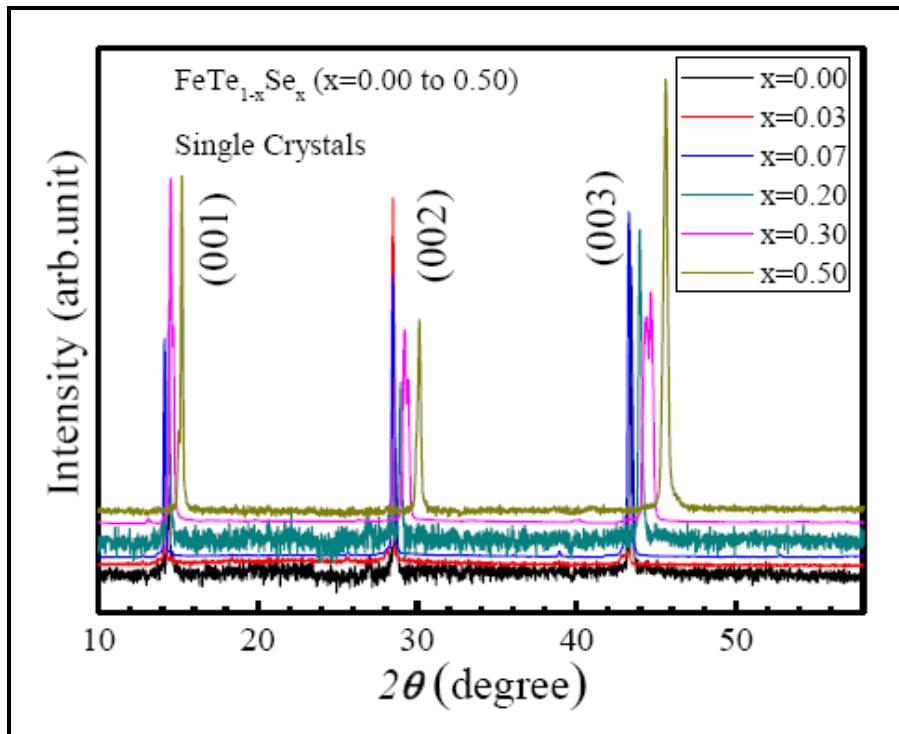


Figure 1: Single crystal XRD pattern for $\text{FeTe}_{1-x}\text{Se}_x$ ($x=0.00$ to 0.50) series at ambient conditions.

Table 1: $\text{FeTe}_{1-x}\text{Se}_x$ ($0.00 \leq x \leq 0.50$) single crystals lattice parameters and coordinate positions using Rietveld refinement.

	$x=0.00$	$x=0.01$	$x=0.03$	$x=0.05$	$x=0.10$	$x=0.30$	$x=0.50$
$a=b$ (Å)	3.8263(2)	3.8267(4)	3.8259(3)	3.824(2)	3.821(3)	3.809(2)	3.801(2)
c (Å)	6.292(4)	6.2858(3)	6.2754(3)	5.272(3)	6.234(3)	6.116(3)	5.998(3)
V (Å ³)	92.118(3)	92.0491(3)	91.8596(2)	91.7467(2)	91.04(2)	88.7816(3)	86.65(3)
Fe	(3/4,1/4,0)	(3/4,1/4,0)	(3/4,1/4,0)	(3/4,1/4,0)	(3/4,1/4,0)	(3/4,1/4,0)	(3/4,1/4,0)
Se	(1/4,1/4,0.286)	(1/4,1/4,0.289)	(1/4,1/4,0.288)	(1/4,1/4,0.289)	(1/4,1/4,0.283)	(1/4,1/4,0.284)	(1/4,1/4,0.286)
Te	(1/4,1/4,0.286)	(1/4,1/4,0.289)	(1/4,1/4,0.288)	(1/4,1/4,0.289)	(1/4,1/4,0.283)	(1/4,1/4,0.284)	(1/4,1/4,0.286)

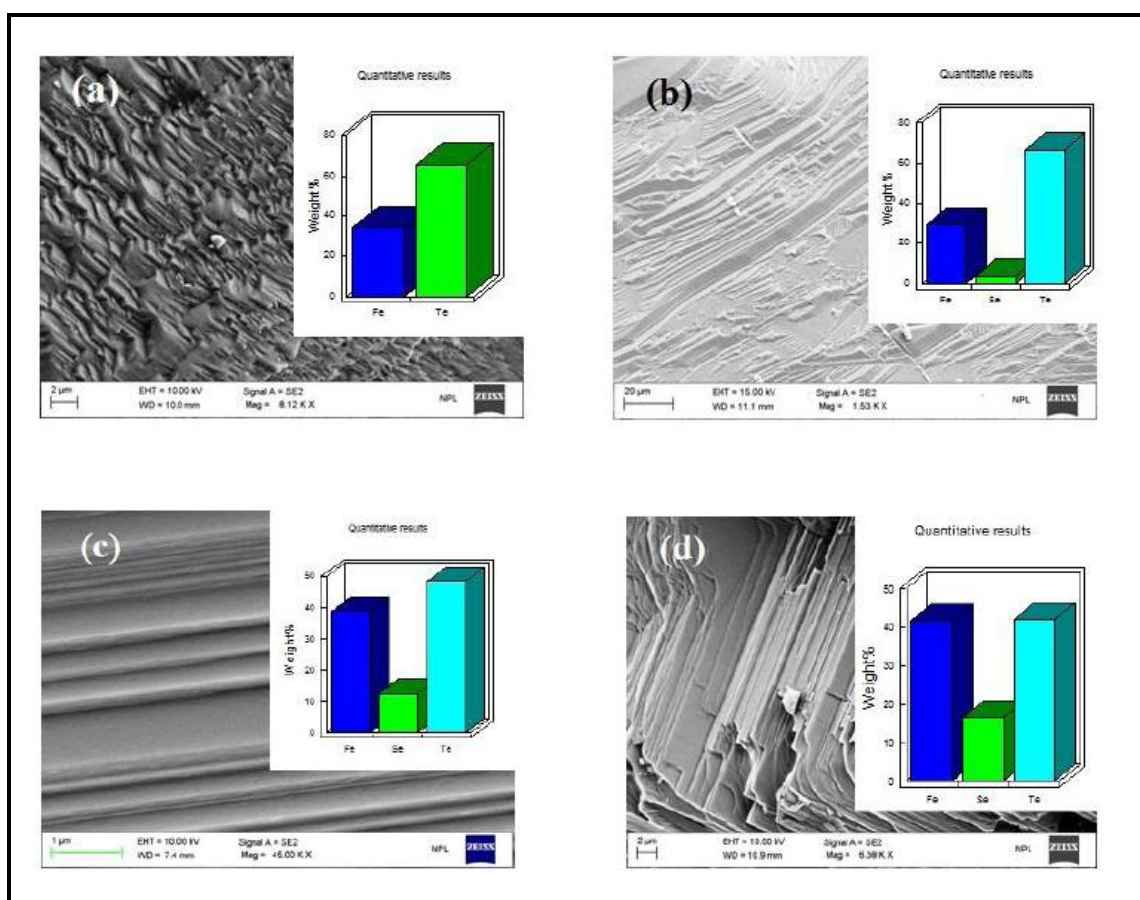


Figure 2: Selected SEM image of $\text{FeTe}_{1-x}\text{Se}_x$ crystals at room temperature (a) FeTe (b) $\text{FeTe}_{0.95}\text{Se}_{0.05}$ (c) $\text{FeTe}_{0.70}\text{Se}_{0.30}$ (d) $\text{FeTe}_{0.50}\text{Se}_{0.50}$. Insets are EDAX of all the samples respectively.

To evaluate the morphology of the synthesized single crystal, SEM observation was performed at room temperature. SEM images of $\text{FeTe}_{1-x}\text{Se}_x$ samples were taken at high

magnification factor for understanding the morphology of the synthesized single crystals, and the results are shown in figure 2(a-d). The SEM image of pure FeTe is shown in Figure 2(a) and the quantitative analysis of the micro relief is presented in the inset. Although the SEM analysis of FeTe was reported elsewhere [32], It is shown for comparison with others crystals. Figure 2(b) and 2(c) show the SEM and EDX analysis of $\text{FeTe}_{0.95}\text{Se}_{0.05}$ and $\text{FeTe}_{0.70}\text{Se}_{0.30}$ crystals, respectively. The results show clearly the layered directionally parallel oriented morphology and elemental composition is found to be close to their stoichiometric ratio. Figure 2(d) depicts the earlier reported $\text{FeTe}_{0.50}\text{Se}_{0.50}$ sample [33] and it is essentially shown for comparison with the other crystals. From the SEM images and EDX, we can conclude that the morphology of all the samples is basically layered type and the elemental compositions are close to starting elemental ratios.

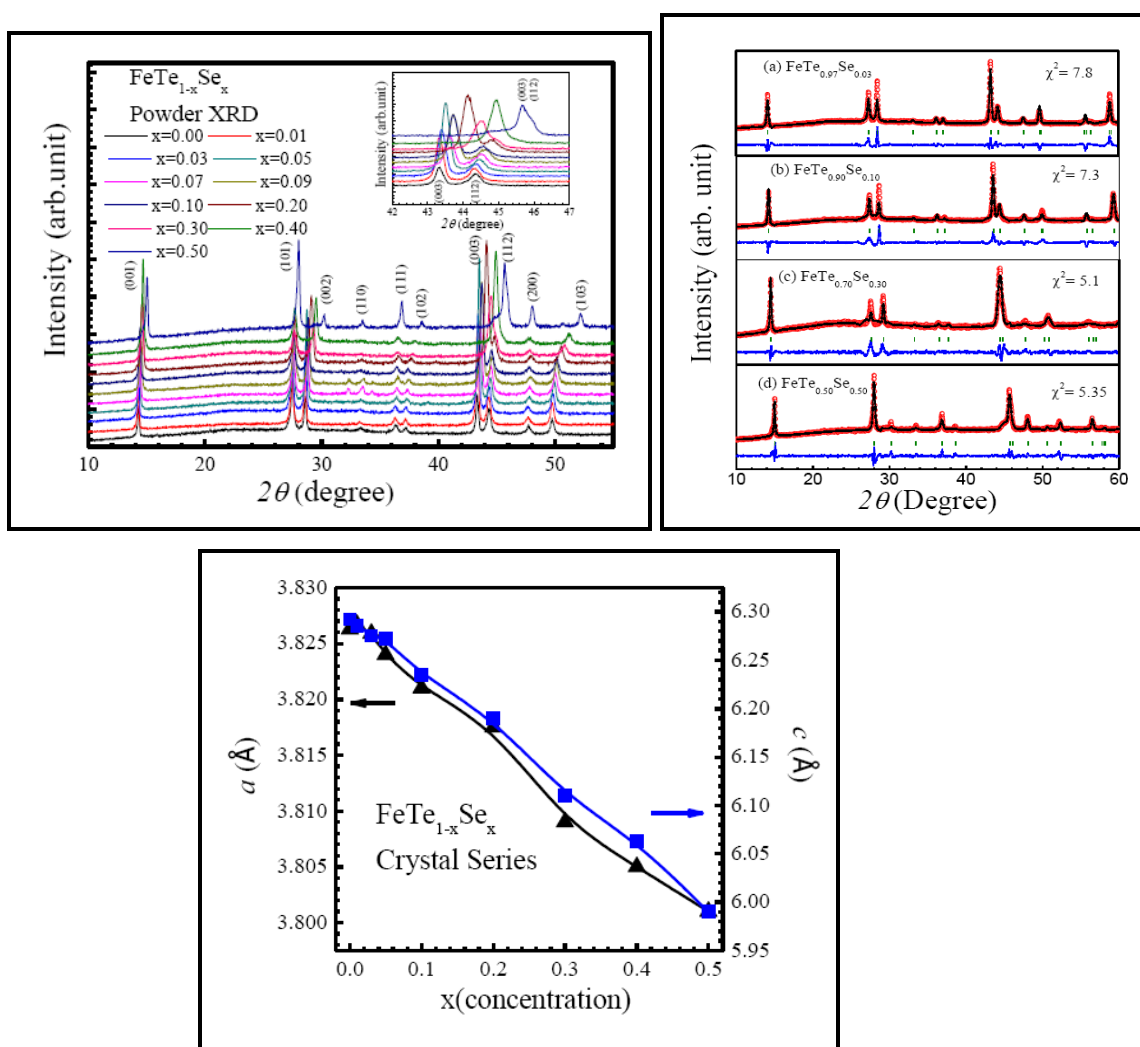


Figure 3: (a) Powder XRD of $\text{FeTe}_{1-x}\text{Se}_x$ ($x=0.00$ to 0.50) series at room temperature. Inset is zoomed part of [003] plane. (b) Observed and Rietveld fitted graph of some of $\text{FeTe}_{1-x}\text{Se}_x$ series samples. (c) Plot between lattice parameters (a and c) with doping concentration (x) of $\text{FeTe}_{1-x}\text{Se}_x$ series.

For further analysis of the $\text{FeTe}_{1-x}\text{Se}_x$ ($0.00 \leq x \leq 0.50$) crystal series, concerning their cell parameters their lattice parameters, coordinate position etc., gently crushed powder XRD measurement was performed at room temperature, as shown in figure 3(a). All the samples exhibit the tetragonal type crystal structure, in space group P4/nmm without any impurity phase present in the samples. From the powder XRD result, it is clearly seen that $(00l)$ peaks are shifted towards higher angle with Se concentration increase in $\text{FeTe}_{1-x}\text{Se}_x$ ($0.00 \leq x \leq 0.50$) series. This result confines the decrement in c lattice parameter with increasing Se partial occupancy at Te site. The inset of figure 3(a) clearly shows the shift of (003) peak towards higher angle.

The Rietveld refinement of powder XRD result was performed using fullprof software, and the observed and fitted plots of selected samples are shown in figure 3(b). The main refinement parameters are given in table 1. The results show the decrement in a and c parameters with increasing Se concentration in $\text{FeTe}_{1-x}\text{Se}_x$ series. As compared to a cell parameter, c cell parameter decreases sharply, which can be clearly seen from figure 3(c). In fig 3(c), it can be seen that both lattice parameters a and c decrease from $3.8263(2)\text{\AA}$ to $3.801(2)\text{\AA}$ and $6.292(4)\text{\AA}$ to $5.998(3)\text{\AA}$ respectively for $x=0.00$ to $x=0.50$. Respectively, fractional volume decreases with increasing Se concentration at Te site in $\text{FeTe}_{1-x}\text{Se}_x$ series.

For understanding the transport properties of the studied crystals, resistivity (ρ) verses temperature (T) measurements are performed from 300K to 2K for $\text{FeTe}_{1-x}\text{Se}_x$ ($0.00 \leq x \leq 0.50$) samples. The ρ - T dependencies are shown in figure 4(a). In $\text{FeTe}_{1-x}\text{Se}_x$ ($0.00 \leq x \leq 0.50$) series, for $x=0.0$ to 0.05 , the known structural/magnetic (T_N) phase transition occurs in ρ - T measurement during cooling and warming cycles. For $x=0$, the transition occurs in resistivity measurement at $\sim 65\text{K}$, while for $x=0.05$ it occurs at $\sim 53\text{K}$. Further details about these crystals i.e. $x=0.00$ to 0.05 are shown elsewhere [32, 34]. There is no superconducting transition i.e., neither T_c^{onset} nor T_c^{offset} ($\rho=0$) occur for $0.0 \leq x \leq 0.05$ samples. Interestingly, for $x=0.07$ both structural/magnetic and superconducting transition T_c^{onset} occurs approximately at 50K and 10K respectively. The superconducting transition temperature T_c increases from 10K for $x=0.07$ to 14K for $x=0.50$ with Se doping in $\text{FeTe}_{1-x}\text{Se}_x$ series.

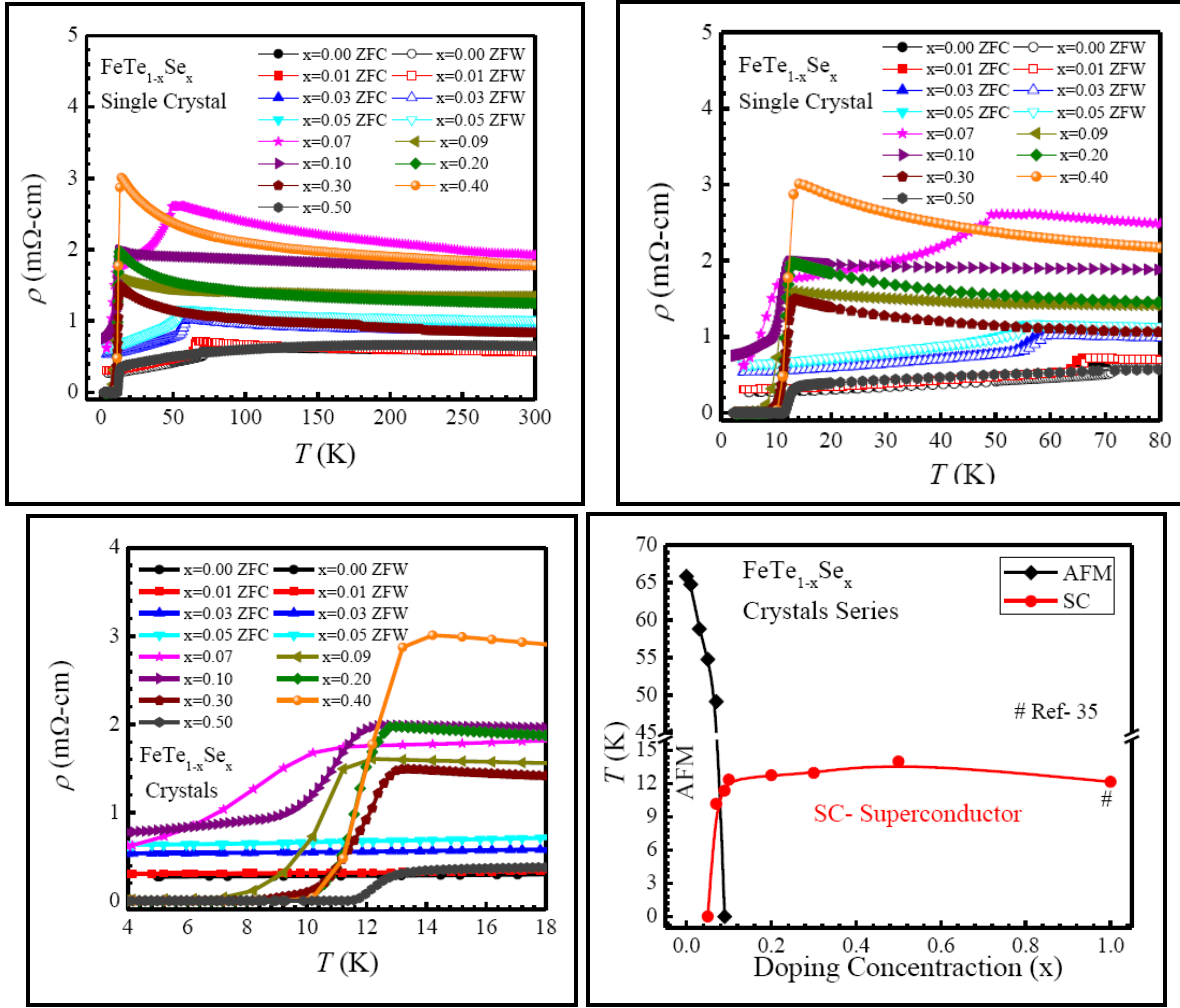


Figure 4: Electrical resistivity (ρ) versus temperature (T) plots for $\text{FeTe}_{1-x}\text{Se}_x$ ($x=0.00$ to 0.50) series (a) Temperature range from 300K to 2K. (b) Temperature range from 80K to 2K. (c) Temperature range from 18 to 4K. (d) Phase diagram of $\text{FeTe}_{1-x}\text{Se}_x$ ($x=0.00$ to 1.00) crystal series, which shows anti-ferromagnetism (AFM) and superconducting (SC) regions.

Figure 4(b) shows zoomed part of figure 4(a) in the range of 80 to 2K. In this figure, one can clearly see that for $x=0.00$, T_N occurs nearly at around 70K in ρ - T measurement with hysteresis of nearly 5K during cooling and warming cycle, being occurring due to presence of latent heat during transition. It is clear from figure 4(b) that T_N decreases with increasing Se up to $x=0.07$ in $\text{FeTe}_{1-x}\text{Se}_x$ series and higher concentration lead towards superconducting transition at low temperature. From figure 4(b), we can conclude that up to $x=0.05$ neither T_c^{onset} nor T_c^{offset} ($\rho=0$) is

seen down to 2K while for $x=0.07$ only T_c^{onset} is occurred at nearly 10K. Also the hysteresis in ρ - T measurement near T_N is seen up to $x=0.05$ crystals during cooling/warming cycles, some of these results are reported earlier [32, 34]. Here, the aim is to fill up the gaps and present the complete phase diagram of $\text{FeTe}_{1-x}\text{Se}_x$ ($x=0.0$ to 0.50) single crystal series.

Table 2: $\text{FeTe}_{1-x}\text{Se}_x$ ($x=0.00$ to 0.50) single crystals, phase transition temperature (T_N) and superconducting transition temperature (T_c^{onset})

x	T_N (K)	T_c^{onset} (K)
0.00	65.84	-
0.01	64.77	-
0.03	58.81	-
0.05	54.78	-
0.07	49.17	10.18
0.10	-	11.38
0.20	-	12.37
0.30	-	12.76
0.50	-	12.97
#1.00	-	12.17

Ref- 35

Figure 4(c) shows the ρ - T measurement from 18 to 4K, i.e. zoomed part of figure 4(a). From this figure, we can say that that maximum T_c is found for $x=0.50$ sample i.e. $\text{FeSe}_{0.50}\text{Te}_{0.50}$ crystal. The T_c^{onset} for $x=0.50$ is at nearly 14K and $T_c^{\text{offset}}(\rho=0)$ is at 12K. More detailed analysis of $\text{FeSe}_{0.50}\text{Te}_{0.50}$ single crystal was reported earlier [33]. The values of phase transition temperature (T_N) and superconducting transition temperature (T_c^{onset}) of $\text{FeTe}_{1-x}\text{Se}_x$ series are shown in table 2. From Table 2, we conclude that maximum T_N is found nearly 65K for $x=0.00$ and maximum T_c is found at 14K for $x=0.50$ crystal. The suggested temperature-doping concentration phase diagram of $\text{FeTe}_{1-x}\text{Se}_x$ ($x=0.00$ to 1.0) series from our results is shown in figure 4(d). The detailed analysis of $x=1.0$ sample is reported earlier [35], and the related point is marked by # in fig 4(d) also. From fig 4(d), one can say that for $x \leq 0.07$, the FeSe/Te system shows the anti-ferromagnetism (AFM) ordering and, for $x \geq 0.07$ this system shows the superconducting (SC) state at low temperature. Interestingly, the $x=0.07$ shows both AFM and SC state at nearly 50K and 10K, respectively. So, from the suggested phase diagram, as Se concentration increases in $\text{FeTe}_{1-x}\text{Se}_x$ series, AFM ordering suppresses and superconductivity appears. Also, the crystals with Se content of $x=0.07$ show both AFM and SC states.

To further study superconducting response of studied $\text{FeTe}_{0.80}\text{Se}_{0.20}$ single crystal, ρ - T measurement was performed under applied magnetic up to 14Tesla. The similar data for $x = 0.50$ crystal were already reported earlier [33]. Figure 5(a) shows the ρ - T behavior of $\text{FeTe}_{0.80}\text{Se}_{0.20}$

single crystal under applied magnetic field up to 14Tesla. From figure 5(a), we can judge the robustness of superconductivity against the magnetic field as the $T_c^{\text{offset}}(\rho=0)$ is only decreased from 10K to 5.5K for zero and 14Tesla magnetic fields respectively. The calculated dT_c/dH for $\text{FeTe}_{0.80}\text{Se}_{0.20}$ sample comes out to be around 0.32K/Tesla. The low dT_c/dH value in the studied crystal signifies the superconductivity robustness to magnetic field up to 14Tesla.

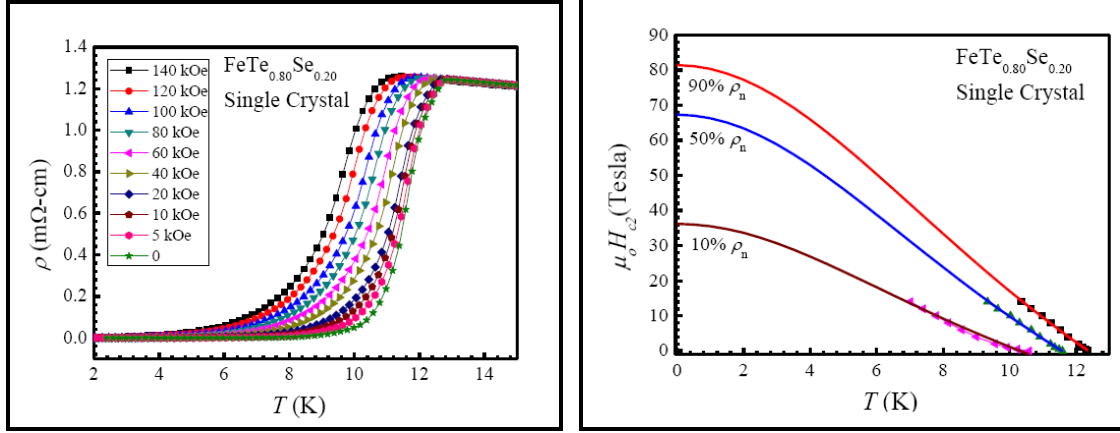


Figure 5: (a) $\rho(T, H)$ under various magnetic fields up to 14Tesla for $\text{FeTe}_{0.80}\text{Se}_{0.20}$ single crystal (b) Upper critical field (H_{c2}) is calculated from $\rho(T, H)$ data with 90%, 50% and 10% normalized resistivity (ρ_n) criteria of $\text{FeTe}_{0.80}\text{Se}_{0.20}$ single crystal.

For further analysis on $\rho(T, H)$ measurement for $\text{FeTe}_{0.80}\text{Se}_{0.20}$ crystal, the upper critical field $H_{c2}(0)$ is calculated using 10%, 50% and 90% normalized resistivity (ρ_n) criterion, which is shown in figure 5(b). The H_{c2} at absolute zero temperature is calculated by extrapolating the curve fitting the data using the Ginzburg Landau (GL) equation $H_{c2}(T) = H_{c2}(0)[(1 - t^2)/(1 + t^2)]$, here $t = T/T_c$ is defined as reduced temperature. The calculated values are found to be nearly 80Tesla, 70Tesla and 35Tesla for $\text{FeTe}_{0.80}\text{Se}_{0.20}$ single crystal at 90%, 50% and 10% ρ_n criterion respectively. High value of H_{c2} for the superconductor leads towards the robustness against applied external magnetic field. The calculated value of H_{c2} for $\text{FeTe}_{0.80}\text{Se}_{0.20}$ single crystal is very high and it is far away from the Pauli Paramagnetic limit, i.e. 1.84 times of T_c [36]. The coherence length $[\xi(0)]$ can be calculated using the value of $H_{c2}(0)$ by the defined equation i.e. $H_{c2}(0) = \Phi_0/2J\xi(0)^2$, where Φ_0 is defined as flux quantum, whose value is $2.0678 \times 10^{-15} \text{ Tesla}\cdot\text{m}^2$. At absolute zero temperature, $\xi(0)$ calculated by the equation is around 20.3\AA for $\text{FeTe}_{0.80}\text{Se}_{0.20}$ single crystal.

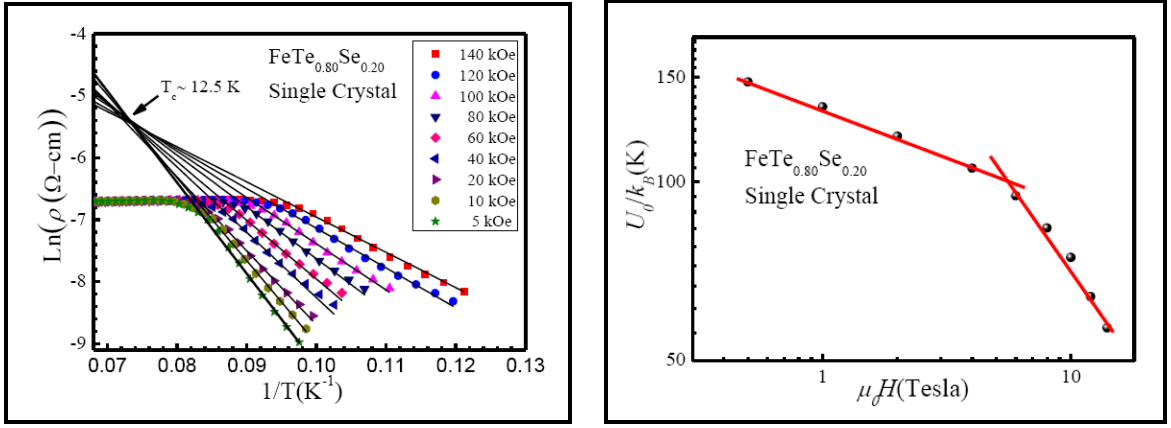


Figure 6: (a) $\ln\rho(T,H)$ vs $1/T$ for various magnetic fields up to 14Tesla for $\text{FeTe}_{0.80}\text{Se}_{0.20}$ single crystal corresponding linear fitted solid line of Arrhenius relation. (b) Thermally Activation energy $U_0(H)$ with solid lines fitted of $U_0(H) \sim H^\alpha$ up to 14Tesla magnetic field for $\text{FeTe}_{0.80}\text{Se}_{0.20}$ single crystal.

Then, the thermally activated flux flow (TAFF) analysis is implemented on $\text{FeTe}_{0.80}\text{Se}_{0.20}$ sample. The dependence of $\text{Ln}\rho$ verses $1/T$ under magnetic fields of up to 14Tesla is shown in figure 6(a). By the TAFF theory [37,38], the TAFF region can be described with the help of Arrhenius relation [39] $\text{Ln}\rho(T, H) = \text{Ln}\rho_0(H) - U_0(H)/k_B T$, where $\text{Ln}\rho_0(H)$ is temperature dependent constant, $U_0(H)$ is thermally activation energy and k_B is the Boltzmann constant. From the Arrhenius equations we can conclude that $\text{Ln}\rho(T, H)$ verses $1/T$ graph would be linearly fitted in TAFF region, as shown in the figure 6(a). Figure 6(a) described that $\text{Ln}\rho(T, H)$ verses $1/T$ and linearly fitted plotted in TAFF region up to 14Tesla magnetic field. In this figure, it can be seen that all the linear fitted extrapolation lines correspondent to magnetic field intercepted at same point, this point nearly coincides with superconducting transition temperature (T_c) of $\text{FeTe}_{0.80}\text{Se}_{0.20}$ sample, i.e. 13K. There is an occurrence of resistivity broadening pattern with applied magnetic field in $\text{FeTe}_{0.80}\text{Se}_{0.20}$ single crystal due to thermally assisted flux motion [40] and is very similar to our previous result for another superconducting $\text{FeSe}_{0.50}\text{Te}_{0.50}$ crystal [33].

The thermal activation energy was calculated for different magnetic fields for $\text{FeTe}_{0.80}\text{Se}_{0.20}$ single crystal, the Ln scale plot between $U_0(H)$ verses magnetic field is shown in figure 6(b). Thermally activation energy is field dependent energy which follows the power law relation with magnetic field, i.e. define as $U_0(H)=K \times H^\alpha$, where $U_0(H)$ is thermally activation energy, K is constant and α is a field dependent constant. For the studied $\text{FeTe}_{0.80}\text{Se}_{0.20}$ single crystal the value of α is found 0.16 up to magnetic field of 4Tesla and 0.60 for higher magnetic fields from 6Tesla to 14Tesla range. This result indicates that single vortex pinning [38] is effective at low field for

FeTe_{0.80}Se_{0.20} single crystal. The thermal activation energy for FeTe_{0.80}Se_{0.20} single crystal varies from 12 to 4.6meV with magnetic field from 0.5 to 14Tesla respectively. The calculated thermal activation energy for FeTe_{0.80}Se_{0.20} crystal is quite low in comparison to FeTe_{0.50}Se_{0.50} single crystal [33]. This shows that the superconductivity robustness for x=0.20 crystal is lower than that for x=0.50 [33].

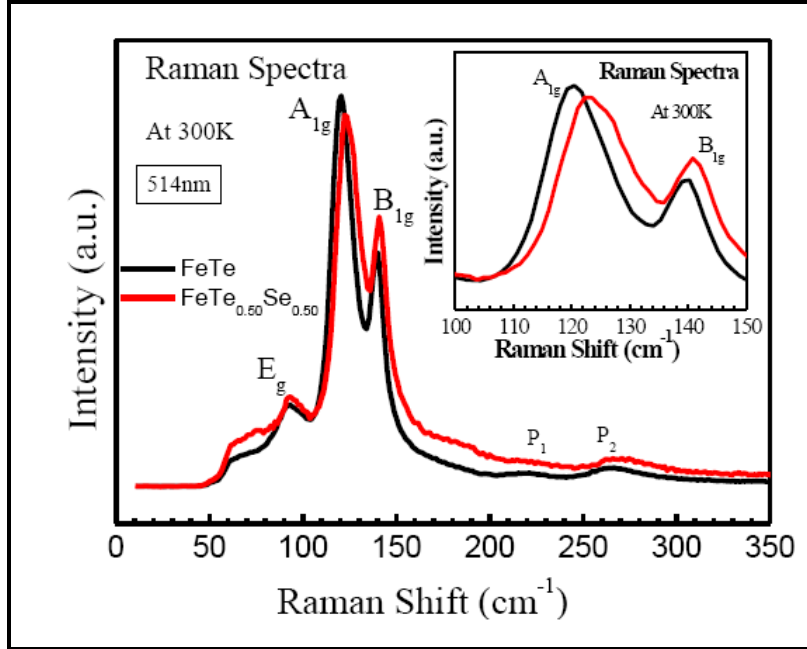


Figure 7: Raman spectra of FeTe_{1-x}Se_x (x=0.00 and 0.50) series at room temperature. Inset is zoomed part of same.

In figure 7, the Raman spectra are shown as recorded for FeTe_{1-x}Se_x (x=0.00 and 0.50) series at room temperature at the laser beam excitation of 514nm with laser power of 25mW. At this power Raman spectra shows the best signal/noise ratio. The Raman spectra were recorded in low wave number range of 50-350cm⁻¹. In the low frequency range for the Fe(Se/Te) system after taking symmetry concern, four Raman active modes (E_g¹, A_{1g}, B_{1g} and E_g²) are expected [41,42]. These modes E_g¹, A_{1g}, B_{1g} and E_g² are attributed to Te/Se, Te/Se, Fe and Fe atom vibrations, respectively. Xia et al [41] explained the A_{1g}(Te) and B_{1g}(Fe) modes in low wave number range (100-200cm⁻¹) of FeTe crystal. In bulk FeSe_{0.82} system, P. Kumar et al [42] observed two Raman modes attributed to E_g (106cm⁻¹) and A_{1g}(160cm⁻¹) in the 100-200cm⁻¹ region. In frequency range of 100-200cm⁻¹, same peaks were observed by Lopes et al [26], as well as in FeSe_{0.50}Te_{0.50} single crystal, at both 300 and 77K. In our Raman spectra recorded for FeTe and FeTe_{0.50}Se_{0.50} crystals, we also found two Raman modes in low wave number region of 100-200cm⁻¹, that is very close to previous literature

results for $\text{FeTe}_{0.50}\text{Se}_{0.50}$ [26]. In figure 7, the Raman spectra of FeTe and $\text{FeTe}_{0.50}\text{Se}_{0.50}$ crystals at room temperature, are shown in the wave number range of $50\text{-}200\text{cm}^{-1}$. Three clear Raman modes are seen which are attributed to $E_g(\text{Te/Se})$, $A_{1g}(\text{Te/Se})$ and $B_{1g}(\text{Fe})$ at 92 , 121 and 140cm^{-1} respectively. Further, two weak Raman modes (P1 and P2) are observed in the range of $200\text{-}300\text{cm}^{-1}$, which are similar to ones being observed by Lopes et al [26]. We also observed slight shifting in the positions of Raman active modes towards higher wave numbers with increasing Se concentration at Te sites in $\text{FeTe}_{1-x}\text{Se}_x$. In the inset of fig. 7, the zoomed part of wave number range ($100\text{-}150\text{cm}^{-1}$) is given to show the Raman peak shifting by Se doping. The Raman mode shifting may be due to lower atomic mass of Se, as compared to Te, and less strong bonding force of $\text{FeSe}_{0.50}\text{Te}_{0.50}$, as compared to FeTe .

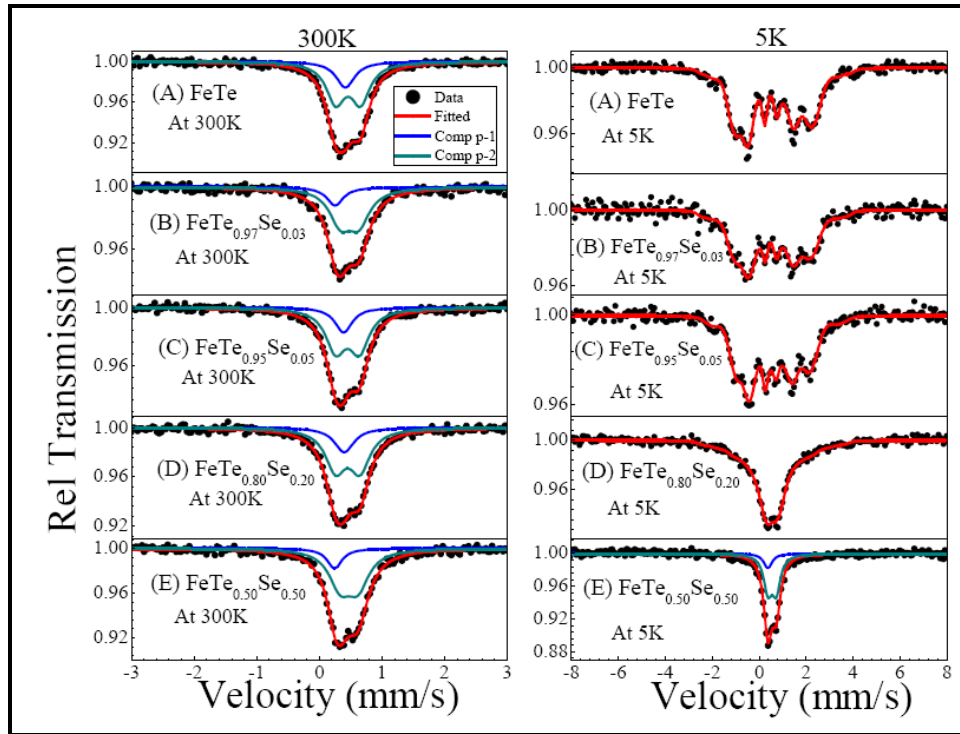


Figure 8: Mossbauer spectra of $\text{FeTe}_{1-x}\text{Se}_x$ ($x=0.00$ to 0.50) crystal series, the left side frame is at 300K (RT) and right side is at 5K temperature.

The Mossbauer spectra of $\text{FeTe}_{1-x}\text{Se}_x$ ($x=0.00$ to 0.50) at room temperature (RT, 300K) and lowest temperature of 5K are shown in left and right side frames of figure 8. For comparison, the Mossbauer spectra for $x=0.00$ sample from our previous study [43] are also provided. At the lowest measurement temperature (5K), the Mossbauer spectra display clear magnetic sextet till 0.05 and a broad doublet for $x=0.20$ indicating the presence of magnetic ordering in these crystals. Therefore, the 5K spectra of these crystals are analyzed with distribution of hyperfine fields and, for $x=0.20$ the data are analysed with doublet along with distribution of hyperfine fields.

The average hyperfine field is found to be 10.6(1), 10.2(1), 9.1(1) and 6.1(1) Tesla for $x=0.0, 0.03, 0.05$ and 0.20 samples, respectively. For higher doping ($x=0.50$), no sextet is observed at 5K, that can be attributed to clear absence of magnetic ordering in this crystal, as supported by $\rho(T)$ measurements. Clearly, successive doping of Se in FeTe results in suppression of magnetic nature, as revealed by Mossbauer spectra at 5K. The $x=0.07$ and 0.20 crystals both have magnetic and superconductivity co-existence.

Conclusion

The $\text{FeTe}_{1-x}\text{Se}_x$ ($0.00 \leq x \leq 0.50$) single crystals were successfully grown from self fluxes in a simple programmable furnace. The structural properties are characterized by XRD and SEM techniques. The cell parameters a and c decrease with Se concentration increase in $\text{FeTe}_{1-x}\text{Se}_x$ series. The magneto transport measurements down to 2K indicate that structural/magnetic phase transition occurs for $\text{FeTe}_{1-x}\text{Se}_x$ series up to $x=0.07$ and superconducting transition occurs for $x \geq 0.07$, although $x=0.07$ show both magnetic and superconducting transition at low temperatures. Highest T_c of around 14K is found for $x=0.50$ sample. Raman and Mossbauer spectroscopy results are also reported for all the crystals and phase diagram of $\text{FeTe}_{1-x}\text{Se}_x$ single crystal series is completed by filling in the gaps with our previous studies [29-32].

Acknowledgement

Authors would like to thank their Director NPL India for his keen interest in the present work. This work is financially supported by the DAE-SRC outstanding investigator award scheme on search for new superconductors. P. K. Maheshwari thanks CSIR, India for research fellowship and AcSIR- Ghaziabad for Ph.D. registration. The authors would like to thanks Mrs. Shaveta Sharma for Raman studies.

References

1. F. C. Hsu, J. Y. Luo, K. W. Yeh, T. K. Chen, T. W. Huang, P. M. Wu, Y. C. Lee, Y. L. Huang, Y. Y. Chu, D. C. Yan and M. K. Wu, PNAS **105**, 14262 (2008).
2. K. W. Yeh, T. W. Huang, Y. L. Huang, T. K. Chen, F. C. Hsu, P. M. Wu, Y. C. Lee, Y. Y. Chu, C. L. Chen, and J. Y. Luo, Euro. Phys. Lett. **84**, 37002 (2008).
3. Y. Kamihara, H. Hiramatsu, M. Hirano, R. Kawamura, H. Yanagi, T. Kamiya, and H. Hosono, J. Am. Chem. Soc. **128**, 10012 (2006).
4. Y. Kamihara, T. Watanabe, M. Hirano, and H. Hosono, J. Am. Chem. Soc. **130**, 3296 (2008).

5. Ren Zhi-An, Lu Wei, Yang Jie, Yi Wei, Shen Xiao-Li, Zheng-Cai, Che Guang-Can, Dong Xiao-Li, Sun Li-Ling, Zhou Fang and Zhao Zhong-Xian, *Chin. Phys. Lett.* **25**, 2215 (2008).
6. X. H. Chen, T. Wu, G. Wu, R. H. Liu, H. Chen and D. F. Fang, *Nature* **453**, 761 (2008).
7. E. Dagotto, *Rev. Mod. Phys.* **66**, 763(1994).
8. D. J. Scalapino, *Phys. Rep.* **250**, 329(1995).
9. M. H. Fang, H. M. Pham, B. Qian, T. J. Liu, E. K. Vehstedt, Y. Liu, L. Spinu, and Z. Q. Mao, *Phys. Rev. B* **78**, 224503 (2008).
10. Y. Mizuguchi, F. Tomioka, S. Tsuda, T. Yamaguchi and Y. Takano, *Appl. Phys. Lett.* **94**, 012503 (2009).
11. R. Hu, E. S. Bozin, J. B. Warren, and C. Petrovic, *Phys. Rev. B* **80**, 214514 (2009).
12. X. Lai, H. Zhang, Y. Wang, X. Wang, X. Zhang, J. Lin, and F. Huang, *J. Am. Chem. Soc.*, **137**, 10148 (2015).
13. Y. Mizuguchi, K. Deguchi, Y. Kawasaki, T. Ozaki, M. Nagao, S. Tsuda, T. Yamaguchi and Y. Takano, *J. Appl. Phys.* **109**, 013914 (2011).
14. S. Li, C. de la Cruz, Q. Huang, Y. Chen, J.W. Lynn, J. Hu, Y. L. Huang, F. C. Hsu, K.W. Yeh, M. K. Wu, and P. Dai, *Phys. Rev. B* **79**, 054503 (2009).
15. A. V. Fedorchenko, G. E. Grechnev, V. A. Desnenko, A. S. Panfilov, S. L. Gnatchenko, V. Tsurkan, J. Deisenhofer, A. Loidl, O. S. Volkova and A. N. Vasiliev, *J. Phys.: Condens. Matter* **23**, 325701 (2011).
16. K. Deguchi, Y. Takano and Y. Mizuguchi, *Sci. Technol. Adv. Mater.* **13**, 054303 (2012).
17. Y. Mizuguchi, F. Tomioka, S. Tsuda, T. Yamaguchi, and Y. Takano, *Appl. Phys. Lett.* **93**, 152505 (2008).
18. S. Masaki, H. Kotegawa, Y. Hara, H. Tou, K. Murata, Y. Mizuguchi, and Y. Takano, *J. Phys. Soc. Jpn.* **78**, 063704 (2009).
19. T. Imai, K. Ahilan, F. L. Ning, T. M. McQueen, and R. J. Cava, *Phys. Rev. Lett.* **102**, 177005 (2009).
20. E.W. Scheidt, V.R. Hathwar, D. Schmitz, A. Dunbar, W. Scherer, F. Mayr, V. Tsurkan, J. Deisenhofer, and A. Loidl, *Eur. Phys. J.B.* **85**, 279 (2012).
21. An-min Zhang, Tian-long Xia, Kai Liu, Wei Tong, Zhao-rong Yang & Qing-ming Zhang, *Scientific Reports*, **3**,1216 (2013).
22. S. He, J. He, W. Zhang, L. Zhao, D. Liu, X. Liu, D. Mou, Y.-B. Ou, Q.-Y. Wang, Z. Li, L. Wang, Y. Peng, Y. Liu, C. Chen, L. Yu, G. Liu, X. Dong, J. Zhang, C. Chen, Z. Xu, X. Chen, X. Ma, Q. Xue and X. J. Zhou, *Nature Materials*, **12**, 605 (2013).
23. Jian-Feng Ge, Zhi-Long Liu, Canhua Liu, Chun-Lei Gao, Dong Qian, Qi-Kun Xue, Ying Liu and Jin-Feng Jia, *Nature Materials*, **24**, 285 (2015).
24. A. Subedi, L. Zhang, D. J. Singh, and M. H. Du, *Phys. Rev. B*, **78**, 134514 (2008).

25. G. F. Chen, Z. G. Chen, J. Dong, W. Z. Hu, G. Li, X. D. Zhang, P. Zheng, J. L. Luo, and N. L. Wang, *Phys. Rev. B*, **79**, 140509(R) (2009).
26. C. S. Lopes, C. E. Foerster, F. C. Serbena, P. R. Junior, A. R. Jurelo, J. L. P. Junior, P. Pureur and A. L. Chinelatto, *Supercond. Sci. Technol.* **25**, 025014 (2012).
27. T. M. McQueen, Q. Huang, V. Ksenofontov, C. Felser, Q. Xu, H. Zandbergen, Y. S. Hor, J. Allred, A. J. Williams, D. Qu, J. Checkelsky, N. P. Ong, and R. J. Cava, *Phys. Rev. B* **79**, 014522 (2009).
28. B.C. Sales, A.S. Sefat, M.A. McGuire, R.Y. Jin, Y.D. Mandrus, *Phys. Rev. B* **79**, 094521 (2009).
29. S. Yu. Sarkisov, V. V. Atuchin, T. A. Gavrilova, V. N. Kruchinin, S. A. Bereznya, Z. V. Korotchenko, O. P. Tolbanov and A. I. Chernyshev, *Russ. Phys. J.* **53 (4)**, 346 (2010).
30. V. V. Atuchin, T. A. Gavrilova, K. A. Kokh, N. V. Kuratieva, N. V. Pervukhina and N. V. Surovtsev, *Solid State Comm.* **152**, 1119 (2012).
31. K. A. Kokh, V. V. Atuchin, T. A. Gavrilova, N. V. Kuratieva, N. V. Pervukhina and N. V. Surovtsev, *Solid State Comm.* **177**, 16 (2014).
32. P.K. Maheshwari, R. Jha, B. Gahtori and V.P.S. Awana, *J. Sup. Novel Mag.* **28**, L2893 (2015).
33. P.K. Maheshwari, R. Jha, B. Gahtori and V.P.S. Awana, *AIP Advances* **5**, 097112 (2015).
34. P.K. Maheshwari, R. Jha, B. Gahtori and V.P.S. Awana, *J. Sup. Novel Mag.* **29**, L543 (2016).
35. P.K. Maheshwari, L.M. Joshi, B. Gahtori, A.K. Srivastava, A. Gupta, S.P. Patnaik and V.P.S. Awana, *Mat. Res. Exp.* **3**, 076002 (2016).
36. A.M. Clogston, *Phys. Rev. Lett.* **9**, 266 (1962).
37. T. T. M. Palstra, B. Batlogg, L. F. Schneemeyer, and J. V. Waszczak, *Phys. Rev. Lett.* **61**, 1662 (1988).
38. G. Blatter, M. V. Feigelman, V. B. Geshkenbein, A. I. Larkin, and V. M. Vinokur, *Rev. Mod. Phys.* **66**, 1125 (1994).
39. J. Jaroszynski, F. Hunte, L. Balicas, Y. J. Jo, I. Raicevic, A. Gurevich, D. C. Larbalestier, F. F. Balakirev, L. Fang, P. Cheng, Y. Jia, and H. H. Wen, *Phys. Rev. B* **78**, 174523 (2008).
40. M. Shahbazi, X. L. Wang, C. Shekhar, O. N. Srivastava, and S. X. Dou, *Sup. Sci. & Tech* **23**, 105008 (2010).
41. T. L. Xia, D. Hou, S. C. Zhao, A. M. Zhang, G. F. Chen, J.L. Luo, N. L. Wang, J. H. Wei, Z. Y. Lu and Q. M. Zhang, *Phys. Rev. B*, **79**, 140510(R) (2009).
42. P. Kumar, A. Kumar, S. Saha, D. V. S. Muthu, J. Prakash, S. Patnaik, U. V. Waghmare, A. K. Ganguli and A. K. Sood, *Solid State Commun.* **150**, 557 (2010).
43. P. K. Maheshwari, V. Raghavendra Reddy and V. P. S. Awana, *J. Supercond. Nov. Magn*, **31**, 1659 (2018).